3

Theoretical Modeling of Enlarging Intracranial Aneurysms

S. Baek, K. R. Rajagopal, and J. D. Humphrey

Texas A&M University
Departments of Biomedical and Mechanical Engineering
College Station, USA

Abstract. Rupture of intracranial aneurysms is the leading cause of spontaneous subarachnoid hemorrhage, which results in significant morbidity and mortality. The mechanisms by which intracranial aneurysms develop, enlarge, and rupture are unknown, and it remains difficult to collect the longitudinal patient-based information needed to improve our understanding. We suggest, therefore, that mathematical models hold considerable promise by allowing us to propose and test competing hypotheses on potential mechanisms of aneurysmal enlargement and to compare predicted outcomes with limited clinical information; in this way, we may begin to narrow the possible mechanisms and thereby focus experimental studies. Toward this end, we develop a constrained mixture model for evolving thin-walled, saccular, and fusiform aneurysms and illustrate its efficacy via computer simulations of lesions having idealized geometries. We also present a method to estimate linearized material properties over the cardiac cycle, which can be exploited when solving coupled fluid–solid interactions in a lesion.

3.1 Introduction

Intracranial aneurysms are focal dilatations of the arterial wall that usually occur in or near the circle of Willis, the primary network of vessels that supplies blood to the brain [HUb]. In general, these aneurysms have one of two forms: fusiform lesions, which are elongated dilations of an artery, and saccular lesions, which are local saclike out-pouchings. Despite significant accomplishments in molecular and cell biology as well as clinical advances, intracranial aneurysms remain an enigma: how do they begin, how do they enlarge, and how do they rupture? Rupture of intracranial aneurysms is the leading cause of spontaneous subarachnoid hemorrhage (SAH), which results in high morbidity and mortality rates. Although it has been long thought that material instabilities are responsible for the enlargement of aneurysms, recent nonlinear analyses cast doubt that such instabilities play any role in the natural history (e.g. [KYa]). Rather, recent histopathological data and modeling suggest that aneurysms enlarge due to growth and remodeling of collagen, the primary load-bearing constituent within the wall [HUa]. Note, therefore, that the natural history of intracranial aneurysms consists of at least three phases: pathogenesis, enlargement, and rupture (Figure 3.1). Albeit not well understood, some initial insult to the cerebral artery causes a small out-pouching or dilation of the arterial wall. We suggest that a stress-mediated process of growth

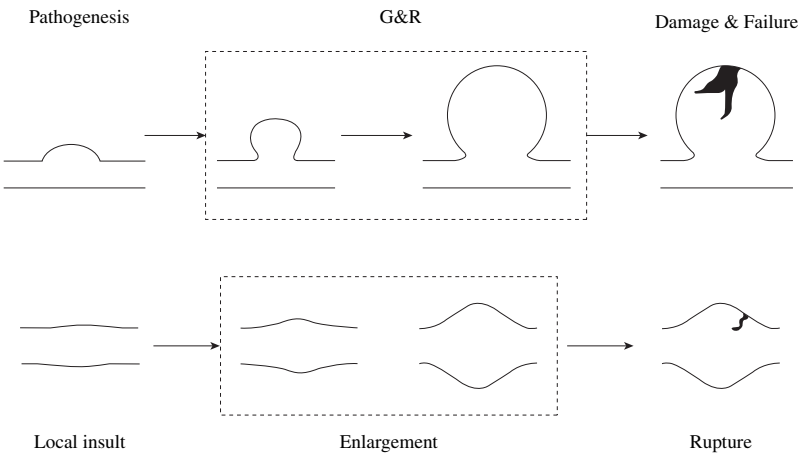

Figure 3.1. Schematic view of the natural history of intracranial saccular (top) and fusiform (bottom) aneurysms.

and remodeling (G&R) is responsible for the subsequent enlargement and possible stabilization of the lesions.

In the early 1980s, Skalak [SKa] first attempted to model growth in soft tissue within the context of finite strain elasticity. His seminal work has been extended by Rodriguez et al. [ROa] and others (e.g. Taber [TAa], Rachev et al. [RAa]), and has served as the primary models of arterial G&R. Briefly, they suggested that shape changes of an unloaded tissue during growth can be decomposed into two fictitious deformations: first, independent growth of stress-free elements of tissue, which need not result in compatible elements, and second, an elastic deformation. The volumetric growth model of Skalak, Rodriguez et al., and others provides a mathematical method to model certain consequences of growth, but it does not model processes by which G&R occur. Recently, Humphrey and Rajagopal [HUc] presented an approach that is conceptually different, one that is based on a fundamental process by which growth and remodeling occur: the continual production and removal of constituents in potentially different stressed configurations. Because the kinetics of turnover and the way each constituent is deposited can differ markedly, they employ ideas from the theory of mixtures to account for the separate contributions of each constituent. Furthermore, because of inherent difficulties in prescribing traction and other boundary conditions in the theory of mixtures, they suggested a constrained mixture model wherein all solid constituents are assumed to have the same motion as that of the mixture despite different natural (stress-free) configurations. Moreover, part of the focus was geometrical alterations due to removal and new production of solid structural constituents as the main mechanism for G&R of soft tissue (see [HUc] for more details).

In this work, we adapt the constrained mixture approach to study the enlargement of intracranial aneurysms and postulate a new potential mechanism of aneurysmal enlargement. In particular, because the medial layer of the aneurysmal wall is degraded during the early development of a lesion and the remaining wall consists primarily of thin layers of collagen, we formulate a constrained mixture model for intracranial aneurysms within the context of a membrane theory. For numerical simulations, we employ initially ellipsoidal and cylindrical membranes for saccular and fusiform aneurysms, respectively. Although soft tissues are dissipative and a proper resolution of any process requires an appropriate thermodynamic framework, at this stage we assume that the body is purely elastic and solve inflation problems with these ideal geometries using the principle of virtual work. We also compare multiple competing hypotheses with regard to the production, removal, and alignment of the collagen fibers. Finally, we recognize that throughout G&R of the aneurysmal wall, hemodynamic loads play key roles, thus fluid–solid interactions should be taken into account. However, a full computation for coupled fluid–solid problems with

a complex geometry and evolving nonlinear properties is even more challenging, requiring considerable computing time and cost. So, at the end of this chapter, we suggest how the theory of small deformations superimposed on large can be exploited when solving coupled fluid–solid interaction problems.

3.2 Theoretical Framework

3.2.1 Kinematics

Let the aneurysmal wall consist of a homogenized[1] mixture of collagen layers having different preferred fiber directions: that is, we treat collagen having different preferred fiber directions as different co-existing constituents (e.g. [CAa,CAb]). The multiple constituents are allowed to have continuous turnover during G&R, but they may have different rates of production and removal. When a new (kth) family of collagen fibers is produced at time $\tau \in (-\infty, t]$, it has a preferred fiber direction that is measured by the in-plane angle $\alpha^k(\tau)$ from the direction of an orthonormal vector in the tangent plane. In general, the in-plane angle for the preferred direction in each constituent can change over time and result in changes in material anisotropy.

In this work, we introduce a fixed configuration κ_R as a computational domain. However, the fixed configuration κ_R is different from the traditional reference configuration in that particles in κ_R can be produced and removed so that the current configuration and the fixed configuration contain the same particles at each time. Now, let the positions of a particle of a lesion (mixture) be $\mathbf{X}$ and $\mathbf{x}$ in the fixed and current configurations of the lesion, and let the mapping χ_{κ_R} assign particles from the fixed configuration to the current configuration at time t, that is,

$$\mathbf{x} = \chi_{\kappa_R}(\mathbf{X}, t). \tag{2.1}$$

The deformation gradient $\mathbf{F}(t)$ is defined through

$$\mathbf{F}(t) := \frac{\partial \chi_{\kappa_R}}{\partial \mathbf{X}}. \tag{2.2}$$

Although all solid constituents are constrained to deform together, we imagine that each constituent has individual natural (i.e. stress-free)

[1] Even within the context of a single constituent inhomogeneous nonlinear elastic body, current procedures that lead to an homogenized model are fraught with serious difficulties (see [SAa])

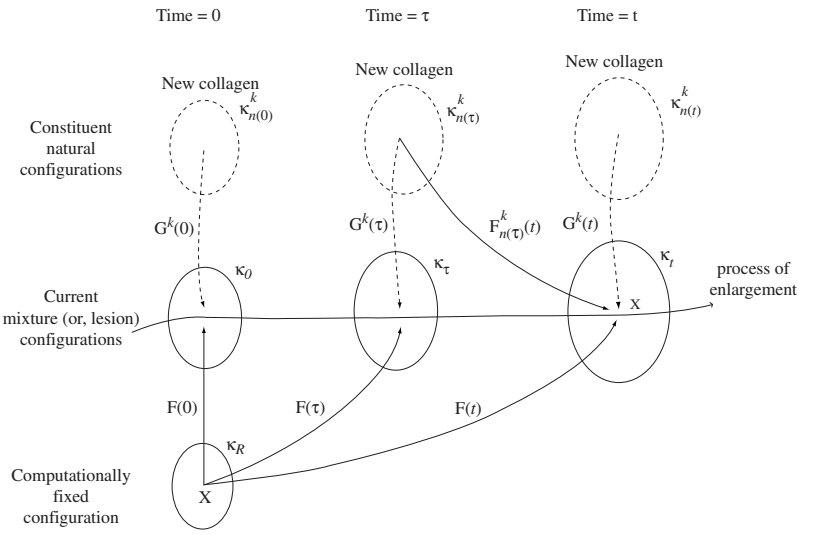

Figure 3.2. Schema of important configurations. The current mixture configurations κ_τ with $\tau \in (0, t]$ track the evolution of a lesion under the physiological condition. For computational purposes, we chose a fixed configuration κ_R where particles are produced and removed so that the current configuration and the fixed configuration contain the same particles at time $\tau \in (0, t]$. Finally, although the newly produced collagen is incorporated into the wall under stress, we imagine the existence of individual natural (stress-free) configurations $\kappa^k_{n(\tau)}$ associated with each instant of production; hence, the natural configurations also evolve.

configurations (see Figure 3.2). Also, if we know how the newly produced collagen fiber is laid down, in the stressed state in which it was produced, then the natural configuration for the newly produced collagen fibers can be inferred. Hence, we postulate that the mechanical properties and the "deposition stretch" of the newly synthesized collagen fibers are always the same; that is, constituents are produced at set homeostatic values in each current configuration (c.f. [HUc, GLa]). Let the prestretch of the kth new constituent be given by a tensor $\mathbf{G}^k(\tau)$, which is associated with a mapping from the natural (i.e. stress-free) configuration of the newly produced kth constituent to the overall loaded configuration κ_τ at time τ (see Figure 3.2). Moreover, let the aneurysmal wall be subjected to a transmural pressure P at time $\tau \in [0, t]$, where t is the current time. Although any configuration in Figure 3.2 can serve as the fixed configuration, we set a traction-free configuration at time $\tau = 0$ as the configuration κ_R, which is convenient computationally. At the time $\tau = t$, the aneurysmal wall

consists of constituents (i.e. families of collagen fibers) that were produced during the period $\tau = -\infty$ to t and survived until the current time t. The deformation gradient for each constituent k at time t, relative to its natural configuration, is $\mathbf{F}^k_{n(\tau)}(t)$, which is associated with mappings of points from the natural configuration of the kth constituent (produced at time τ) to the current configuration. We assume a constrained mixture, that is, the individual constituents must move with the mixture (lesion). Hence, we have (see Figure 3.2)

$$\mathbf{F}^k_{n(\tau)}(t) = \mathbf{F}(t)\mathbf{F}^{-1}(\tau)\mathbf{G}^k(\tau), \tag{2.3}$$

where $\mathbf{F}(\tau)$ and $\mathbf{F}(t)$ are associated with mappings from the fixed configuration to subsequent configurations of the lesion at times τ and t, respectively.

3.2.2 Fibrous Structure

Let $\mathbf{M}^k_{n(\tau)}$ and $\mathbf{m}^k_{n(\tau)}(t)$ be unit vectors in the directions of a family of collagen fibers (i.e. kth constituent produced at time τ) in the natural and loaded configurations, respectively. These unit vectors are related via,

$$\mathbf{m}^k_{n(\tau)}(t) = \frac{\mathbf{F}^k_{n(\tau)}(t)\mathbf{M}^k_{n(\tau)}}{|\mathbf{F}^k_{n(\tau)}(t)\mathbf{M}^k_{n(\tau)}|}. \tag{2.4}$$

The unit vector in the fiber direction in κ_R is thus $\mathbf{M}^k_R(\tau) = (\mathbf{F}^{-1}(\tau)\mathbf{G}^k \mathbf{M}^k_{n(\tau)})/|\mathbf{F}^{-1}(\tau)\mathbf{G}^k\mathbf{M}^k_{n(\tau)}|$. Let $\{\mathbf{E}_1, \mathbf{E}_2\}$ and $\{\mathbf{e}_1, \mathbf{e}_2\}$ be two orthonormal bases in fixed and current configurations, respectively. Also let $\alpha^k(t)$ be the angle between $\mathbf{m}^k_{n(\tau)}(t)$ and $\mathbf{e}_1$, and $\alpha^k_R(\tau)$ be the angle between $\mathbf{M}^k_R(\tau)$ and $\mathbf{E}_1$ for the kth collagen fiber that was produced at time τ. When the principal directions remain principal, the stretch experienced by the kth constituent, along the fiber direction, can be computed as

$$\lambda^k(t) = \sqrt{(\lambda_1 \cos\alpha^k_R)^2 + (\lambda_2 \sin\alpha^k_R)^2}, \tag{2.5}$$

where λ_1 and λ_2 are two principal stretches at any t. Alternatively, the stretch of the kth constituent, relative to its individual fiber direction in the natural configuration $\kappa^k_{n(\tau)}$, is given as

$$\lambda^k_{n(\tau)}(t) = \sqrt{\mathbf{M}^k_{n(\tau)} \cdot \mathbf{F}^k_{n(\tau)}(t)^T \mathbf{F}^k_{n(\tau)}(t)\mathbf{M}^k_{n(\tau)}}. \tag{2.6}$$

As noted above, we assume that a newly produced family of collagen fibers is always incorporated within the wall at a homeostatic stretch; that is, the value of the stretch of the constituent is G_h when it is produced ($\mathbf{G}^k\mathbf{M}^k_{n(\tau)} = G_h\mathbf{m}^k_{n(\tau)}(\tau)$). Of course, the fibers are stretched farther during the enlargement of the lesion, this additional stretch being $\lambda^k(t)/\lambda^k(\tau)$,

where $\lambda^k(\tau)$ and $\lambda^k(t)$ are stretches calculated from the fixed configuration to the pressurized configurations at time τ and time t, respectively. Thus, the stretches of fibers of the kth constituent become

$$\lambda^k_{n(\tau)}(t) = G_h \frac{\lambda^k(t)}{\lambda^k(\tau)}. \tag{2.7}$$

Let the behavior of the kth family of collagen fibers be describable via an exponential-type strain energy function per unit volume in κ_R

$$W^k(\lambda^k_{n(\tau)}) = c\Big\{ \exp\Big[c_1(\lambda^k_{n(\tau)}{}^2 - 1)^2\Big] - 1\Big\}, \tag{2.8}$$

where the material parameters c and c_1 are assumed to be the same for all families.

3.2.3 Kinetics of G&R

The mass of the individual constituents, and thus that of the lesion, changes due to local production and removal of collagen. The total mass per unit area in κ_R at time t, $M(t)$, can be calculated as

$$M(t) = \sum_k M^k(t) = \sum_k \Big[M^k(0) Q^k(t) + \int_0^t m^k(\tau) q^k(t-\tau) d\tau \Big], \tag{2.9}$$

where $m^k(\tau)$ is the rate of production of the kth constituent at time τ per unit area and $q^k(t-\tau)$ is its survival function; that is, the fraction produced at time τ that remains at time t, $Q^k(t)$ is the fraction of the kth constituent that was present at time 0 and still remains at time t (i.e. has not yet been removed). Although we model the aneurysm as a membrane mechanically, we can calculate the thickness in postprocessing. Assuming the overall mass density of the wall remains constant (i.e. $\rho \equiv \rho_o \quad \forall\tau$; [ROa]), the thickness of the wall is given as

$$h(t) = \frac{M(t)}{J\rho}, \tag{2.10}$$

where $J = \det(\mathbf{F}(t))$. Although the transient response to loads applied during the cardiac cycle may be isochoric, volume need not be conserved during G&R.

3.2.4 Stress-Mediated G&R

The production and removal of each constituent results from biological activity. For example, collagen is produced and organized by fibroblasts and degraded by enzymes such as matrix metalloproteinases (or MMPs).

Recent studies show that many cell types (including fibroblasts that populate the aneurysmal wall) can sense and convert mechanical stimuli into biological signals, and thereby effect growth and remodeling. As an example, we postulate that the production of each constituent is a function of the number of cells $n(t)$ per unit reference area and the stress experienced by the cells via the local collagen matrix, namely

$$m^k(t) = n(t)\Big(f^k(\sigma^k(t) - \sigma_h) + f_h\Big), \tag{2.11}$$

where σ^k is a time-averaged (over a cardiac cycle) mean value of a scalar-measure of the stress, and σ_h is a homeostatic value of this stress-measure. Here, we assume

$$\sigma^k(t) = \frac{|\mathbf{T}(t)\mathbf{m}^k_{n(\tau)}(t)|}{h(t)}, \tag{2.12}$$

where $\mathbf{T}(t)$ is the overall membrane stress at time t. If cells proliferate such that cell density (per unit volume in the current loaded configuration) is constant, then the number of the cells increases proportionately with volume changes; that is, $n(t) = n(0)M(t)/M(0)$. A special case allows a linear dependence on the stress difference (cf. [RAa,TAa]), whereby the production rate of a constituent can be expressed as

$$m^k(t) = \frac{M(t)}{M(0)}\Big(K_g(\sigma^k(t) - \sigma_h) + \tilde{f}_h\Big), \tag{2.13}$$

where $\tilde{f}_h$ is f_h multiplied by the initial cell density $n(0)$ and K_g is a scalar parameter that controls the stress-mediated growth. For illustrative purposes, we assume a simple form for the survival function $q(\tilde{\tau})$ in Eq. (2.9). After its production, let there be no removal of a constituent until time t_1 and, then, let the constituent degrade gradually until all of the constituent is removed by time t_2. Toward this end, let

$$q(\tilde{\tau}) = \begin{cases} 1 & 0 \le \tilde{\tau} < t_1 \\ \frac{1}{2}\Big\{\cos\Big(\frac{\pi}{t_2 - t_1}(\tilde{\tau} - t_1)\Big) + 1\Big\} & t_1 \le \tilde{\tau} \le t_2 \\ 0 & t_2 < \tilde{\tau} \end{cases}. \tag{2.14}$$

We introduce a nondimensional parameter for a stress mediation parameter:

$$\hat{K}_g = \left(\frac{\sigma_h t_2}{M(0)}\right) K_g. \tag{2.15}$$

3.2.5 Stress and Strain Energy Function

The total Cauchy membrane stress $\mathbf{T}$ (i.e. tension, or force per current length) is:

$$T_{11}(t) = \frac{1}{\lambda_2(t)}\frac{\partial w}{\partial \lambda_1(t)} \qquad T_{22}(t) = \frac{1}{\lambda_1(t)}\frac{\partial w}{\partial \lambda_2(t)}, \tag{2.16}$$

where w is the strain energy per unit area in the fixed configuration κ_R. We postulate that $w = \sum_k w^k$ and it evolves as

$$w^k(t) = \frac{M^k(0)}{\rho} Q^k(t) W^k(\lambda^k_{n(0)}(t)) + \int_0^t \frac{m^k(\tau)}{\rho} q(t-\tau) W^k(\lambda^k_{n(\tau)}(t)) d\tau, \tag{2.17}$$

where W^k is the aforementioned strain energy of the kth constituent per unit volume and $q^k(\tilde{\tau}) = q(\tilde{\tau})$. Substituting Eq. (2.17) into Eq. (2.16) and using Eq. (2.3), the Cauchy membrane stress is

$$T_{11}(t) = \sum_k \frac{1}{\lambda_2(t)} \Bigg\{ \frac{M^k(0) Q^k(t) G_h}{\rho \lambda^k(0)} \frac{\partial W^k}{\partial \lambda^k_{n(0)}(t)} \frac{\partial \lambda^k(t)}{\partial \lambda_1(t)} + \int_0^t \frac{m^k(\tau) q(t-\tau) G_h}{\rho \lambda^k(\tau)} \frac{\partial W^k}{\partial \lambda^k_{n(\tau)}(t)} \frac{\partial \lambda^k(t)}{\partial \lambda_1(t)} d\tau \Bigg\}, \tag{2.18}$$

$$T_{22}(t) = \sum_k \frac{1}{\lambda_1(t)} \Bigg\{ \frac{M^k(0) Q^k(t) G_h}{\rho \lambda^k(0)} \frac{\partial W^k}{\partial \lambda^k_{n(0)}(t)} \frac{\partial \lambda^k(t)}{\partial \lambda_2(t)} + \int_0^t \frac{m^k(\tau) q(t-\tau) G_h}{\rho \lambda^k(\tau)} \frac{\partial W^k}{\partial \lambda^k_{n(\tau)}(t)} \frac{\partial \lambda^k(t)}{\partial \lambda_2(t)} d\tau \Bigg\}. \tag{2.19}$$

3.3 Simulations for Saccular Aneurysms

3.3.1 Method

We assume axisymmetric ellipsoidal membrane geometries for a saccular aneurysm in both the fixed and current configuration. Furthermore, parametric relations in the fixed configuration can be described by continuous functions $Z = Z(\Phi)$ and $R = R(\Phi)$ (Figure 3.3). We also use two sets of two-dimensional curvilinear coordinates, $\Xi = \{\Phi, \Theta\}$ for the fixed configuration and $\xi = \{\phi, \theta\}$ for the current configuration. The associated bases are given by

$$\mathbf{G}_i = \frac{\partial \mathbf{X}}{\partial \Xi_i}, \qquad \mathbf{g}_i = \frac{\partial \mathbf{x}}{\partial \xi_i}, \tag{3.1}$$

where $i = 1, 2$. Locally orthonormal bases are obtained by

$$\mathbf{E}_i = \frac{\mathbf{G}_i}{|\mathbf{G}_i|}, \qquad \mathbf{e}_i = \frac{\mathbf{g}_i}{|\mathbf{g}_i|} \tag{3.2}$$

and the outward unit normal directions are

$$\mathbf{N} = \frac{\mathbf{G}_1 \times \mathbf{G}_2}{|\mathbf{G}_1 \times \mathbf{G}_2|}, \qquad \mathbf{n} = \frac{\mathbf{g}_1 \times \mathbf{g}_2}{|\mathbf{g}_1 \times \mathbf{g}_2|}. \tag{3.3}$$

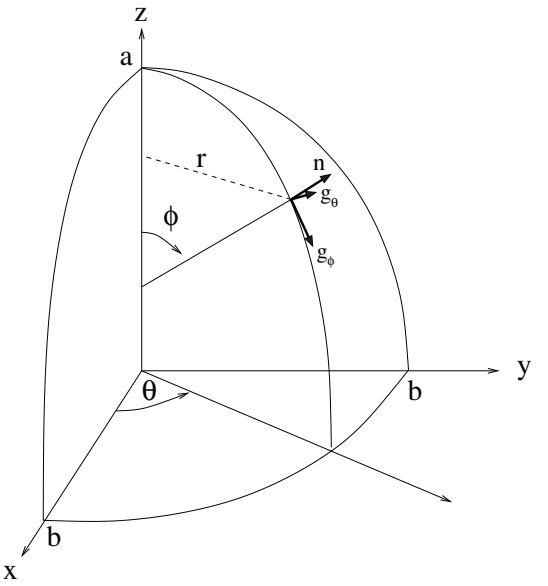

Figure 3.3. Coordinate system for an axisymmetric saccular lesion in a current configuration. Similar values exist for the reference configuration: X, Y, Z, A, B, Θ, Φ, and R.

When the motion due to growth is assumed as

$$\phi = \phi(\Phi) \qquad \theta = \Theta, \tag{3.4}$$

then the components of the 2-D deformation gradient $\mathbf{F} = F_{iJ}\mathbf{e}_i \otimes \mathbf{E}_J$ can be calculated by

$$F_{iJ} = \begin{bmatrix} \frac{h_1}{H_1}\phi' & 0 \\ 0 & \frac{h_2}{H_2} \end{bmatrix} = \begin{bmatrix} \lambda_1 & 0 \\ 0 & \lambda_2 \end{bmatrix}, \tag{3.5}$$

where $(\cdot)' = \partial(\cdot)/\partial\Phi$ and

$$H_1 = \frac{A^2B^2}{(A^2\cos^2\Phi + B^2\sin^2\Phi)^{3/2}}, \qquad H_2 = R \tag{3.6}$$

$$h_1 = \frac{a^2b^2}{(a^2\cos^2\phi + b^2\sin^2\phi)^{3/2}}, \qquad h_2 = r. \tag{3.7}$$

For numerical simulations, we consider an aneurysm approximated as an initially ellipsoidal membrane with two primary axes: dimensions $2A$ for the height and $2B$ for the diameter of the equator. Moreover, let the wall initially consist of two families of fibers (i.e. two constituents) and thus two preferred directions, at 0 and $\pi/2$, and initially the same mass fraction for

both constituents. The strain energy (2.17) is not only a function of the deformation (and thus position) at any time, but also of the past history of the deformations and the rate of mass production. In general, therefore,

$$w(t) = w(\lambda_i(\Phi,t);\, \lambda_i(\Phi,\tau), m^k(\Phi,\tau)), \qquad (i=1,2,\;\; 0 \le \tau < t) \tag{3.8}$$

$$= \hat{w}(\phi(\Phi,t), a(t), b(t); \lambda_i(\Phi,\tau), m^k(\Phi,\tau)), \tag{3.9}$$

where a and b are dimensions in the deformed primary axes. Such inflation problems can be solved using the principle of virtual work, the governing equation for which is

$$\delta I = \int_S \delta w \, dA - \int_s P\mathbf{n} \cdot \delta\mathbf{x} da = 0, \tag{3.10}$$

where $\delta\mathbf{x}$ represents virtual changes in position. The surfaces S and s correspond to the surface area of the fixed and current configuration. Next, let the function $\phi(\Phi)$ be approximated via

$$\phi = \sum_{j=1}^{n} \phi_j \psi_j, \tag{3.11}$$

where ϕ_j is the jth nodal value of $\phi(\Phi)$ and ψ_j is a quadratic interpolation function; a variational procedure for (3.10) with respect to ϕ yields a nonlinear algebraic equation. Using similar approximations for a and b, each yielding associated algebraic equations, we thus formulate the weak form (3.10) as

$$\mathcal{F} \equiv \begin{Bmatrix} 2\pi \displaystyle\int_0^{\Phi_o} \left\{ \frac{\partial w}{\partial \phi}\psi_i + \frac{\partial w}{\partial \phi'}\psi_i{}' \right\} RH_1 d\Phi \\ 2\pi \displaystyle\int_0^{\Phi_o} \left\{ \frac{\partial w}{\partial a} RH_1 - P(r_{,\phi} z_{,a} - z_{,\phi} r_{,a})\phi' r \right\} d\Phi \\ 2\pi \displaystyle\int_0^{\Phi_o} \left\{ \frac{\partial w}{\partial b} RH_1 - P(r_{,\phi} z_{,b} - z_{,\phi} r_{,b})\phi' r \right\} d\Phi \end{Bmatrix} = \begin{Bmatrix} 0 \\ 0 \\ 0 \end{Bmatrix}. \tag{3.12}$$

The nonlinear finite element equations (3.12) are solved using a Newton–Raphson procedure.

3.3.2 Results

To simulate an initial insult, we prescribe a reduction in mass from the total mass of the stable lesion as an initial condition. Such a mass reduction could be caused by a proteolytic weakening of the wall, with an associated loss of elastin and then smooth muscle. Mass reduction induces larger values of stretch in the wall than the homeostatic value and increases wall stress. This initial perturbation initiates enlargement due to G&R in the wall. The enlargement of an ellipsoidal aneurysm is plotted (Figure 3.4) for different

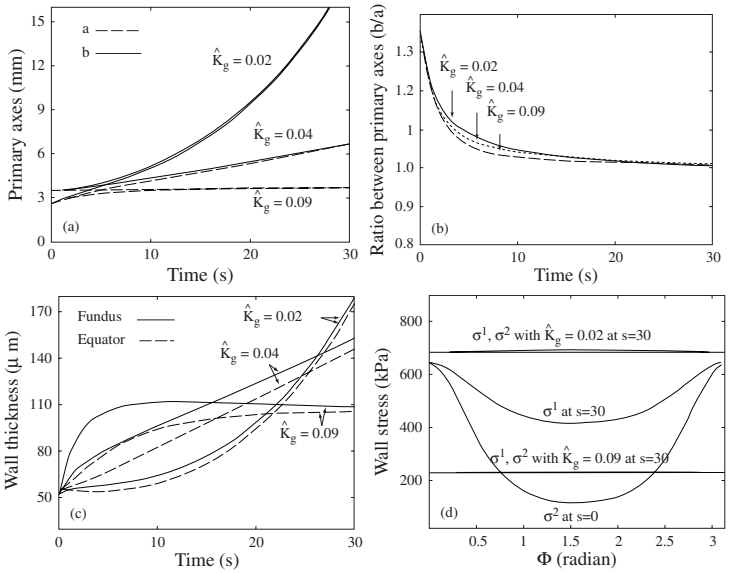

Figure 3.4. G&R of an initially ellipsoidal aneurysm for different values of the parameter K_g for stress mediation. Note that a and b tend to become equal early on (panels a and b), thus yielding a spherical saccular lesion with more uniform wall stress (panel d).

stress mediation parameters $\hat{K}_g$ for a 20% mass reduction. The time scale is normalized by a collagen life span t_2; that is, $s = t/t_2$. The rate of enlargement was higher for a 20% mass reduction than a 5% reduction for the same value of $\hat{K}_g$ (not shown), which suggests that a more severe initial perturbation may cause a faster enlargement of an aneurysm. The rate of enlargement decreases with larger values of $\hat{K}_g$ (Figure 3.4a). When $\hat{K}_g$ is 0.09, the aneurysm quickly reaches its (biologically) stable state and there is no more enlargement. In contrast, when $\hat{K}_g$ is smaller than 0.04, the aneurysm grows in a unbounded manner. Stabilization depends on changes in the ratio of the primary axis (a or b) to the wall thickness h during G&R (recall that the stress in a spherical membrane is $Pa/2h$). For a larger value of $\hat{K}_g$, thickness increases faster than the rate of enlargement, hence wall stress can reach its homeostatic value and the aneurysm can become stable (Figure 3.4c). For a value of $\hat{K}_g$ smaller than 0.04, the ratio between the radius and the thickness keeps increasing, hence the stress increases similarly. When $\hat{K}_g = 0.04$, both radius and thickness increase linearly with respect to time, but the ratio of the radius to the thickness remains nearly constant. Thus the stress also remains the same despite continued enlargement. The tendency toward a spherical shape is similar for all three values of $\hat{K}_g$ (Figure 3.4b). Moreover, this tendency is strong early on, with

lesions becoming almost spherical by $s = 10$. Aneurysmal wall stress thus becomes more uniform over time (Figure 3.4d).

3.4 Simulations for Fusiform Aneurysms

3.4.1 Method

We assume that initial geometries for fusiform aneurysms are axisymmetric cylindrical membranes. The parametric relation in the fixed configuration can be described by continuous functions $R = R(Z)$ (Figure 3.5). The positions of a point in the fixed and current configurations of the lesion, $\mathbf{X}$ and $\mathbf{x}$, can thus be expressed by two sets of cylindrical polar coordinates (Z, θ, R) and (z, θ, r), respectively:

$$\mathbf{X} = R\cos\Theta\mathbf{i} + R\sin\Theta\mathbf{j} + Z\mathbf{k}, \tag{4.1}$$

$$\mathbf{x} = r\cos\theta\mathbf{i} + r\sin\theta\mathbf{j} + z\mathbf{k}. \tag{4.2}$$

We also use a set of two-dimensional curvilinear coordinates, $\Xi_i = \{Z, \Theta\}$ whereby the current position can be expressed by $\mathbf{x} = \mathbf{x}(z(Z, \Theta),$

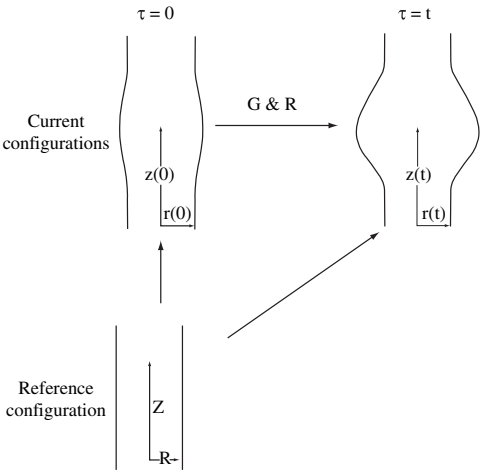

Figure 3.5. Axisymmetric geometries of a fusiform lesion in current (i.e. pressurized) configurations at time $\tau = 0$ and t as well as a convenient unpressurized reference configuration (which need not be stress-free if different families of collagen–proteoglycans are in tension/compression and self-equilibrate).

$\theta(Z,\Theta)$, $r(Z,\Theta)) = \mathbf{x}(Z,\Theta)$. The associated bases and orthonormal bases are given by

$$\mathbf{G}_i = \frac{\partial \mathbf{X}}{\partial \Xi_i}, \qquad \mathbf{g}_i = \frac{\partial \mathbf{x}}{\partial \Xi_i}, \qquad \mathbf{E}_i = \frac{\mathbf{G}_i}{|\mathbf{G}_i|}, \qquad \mathbf{e}_i = \frac{\mathbf{g}_i}{|\mathbf{g}_i|}, \tag{4.3}$$

where $i = 1, 2$. When the deformation due to growth is assumed as

$$z = z(Z), \qquad \theta = \Theta, \qquad r = r(Z), \tag{4.4}$$

then the components of the 2-D deformation gradient $\mathbf{F}(t) = F_{iJ}\mathbf{e}_i \otimes \mathbf{E}_J$, where

$$F_{iJ} = \begin{bmatrix} \lambda_1 & 0 \\ 0 & \lambda_2 \end{bmatrix}, \qquad \lambda_1 = \frac{\sqrt{(z')^2 + (r')^2}}{\sqrt{1 + (R')^2}}, \qquad \lambda_2 = \frac{r}{R}, \tag{4.5}$$

where $(\cdot)' = \partial(\cdot)/\partial Z$. For computations of the enlargement of fusiform aneurysms, we allow the orientation of new collagen to change during G&R. It is not known how the alignment of newly produced collagen is decided, however, thus we consider multiple hypotheses and compare their consequences. Let us define a unit vector for the preferred alignment $\mathbf{e}^p$ and assume that new collagen is deposited with this preferred alignment (similar to Driessen et al. [DRa]). Let the vector $\mathbf{e}^p = f_1\mathbf{e}_1 + f_2\mathbf{e}_2$, where $\mathbf{e}_1$ and $\mathbf{e}_2$ are unit vectors in the axial and circumferential directions, respectively. When f_1 and f_2 are functions of principal stresses, the preferred alignment will be dictated by the mixture stress at each time t. Conversely, when f_1 and f_2 are functions of principal stretches, the preferred alignment will be dictated by the mixture stretch. We compare several cases:

- Case 1: The preferred alignment is dictated by principal stresses, and the angle between $\mathbf{e}^p$ and a principal axis decreases when the principal stress along that axis becomes larger, specifically, $f_1 = \sigma_1/\sqrt{\sigma_1^2 + \sigma_2^2}$ and $f_2 = \sigma_2/\sqrt{\sigma_1^2 + \sigma_2^2}$, where σ_1 and σ_2 are principal stresses in $\mathbf{e}_1$ and $\mathbf{e}_2$ directions, respectively.

- Case 2: The preferred alignment is dictated by the lesser principal stress, thus in contrast to Case 1, let $f_1 = \sigma_2/\sqrt{\sigma_1^2 + \sigma_2^2}$ and $f_2 = \sigma_1/\sqrt{\sigma_1^2 + \sigma_2^2}$.

- Case 3: The preferred alignment is dictated by principal stretches and the angle between $\mathbf{e}^p$ and a principal axis decreases when that principal stretch is larger: $f_1 = \lambda_1/\sqrt{\lambda_1^2 + \lambda_2^2}$ and $f_2 = \lambda_2/\sqrt{\lambda_1^2 + \lambda_2^2}$.

Similar to the simulation for saccular aneurysms, we use the principle of virtual work (3.10). Let functions $r(Z)$ and $z(Z)$ be approximated via

$$r = \sum_{j=1}^{n} r_j \psi_j, \qquad z = \sum_{j=1}^{n} z_j \psi_j, \tag{4.6}$$

where r_j and z_j are the jth nodal values of $r(Z)$ and $z(Z)$, respectively, and n is the number of nodes. The function ψ_j is a global quadratic interpolation function corresponding to the jth node. A variation of Eq. (3.10) with respect to r and z yields two sets of nonlinear algebraic equations:

$$\mathcal{F} \equiv \left\{ \begin{array}{l} 2\pi \int_0^{Z_o} (\frac{\partial w}{\partial r}\psi_i + \frac{\partial w}{\partial r'}\psi_i{}')R\sqrt{1+(R')^2} - Pz'r\psi_i \; dZ \\ 2\pi \int_0^{Z_o} (\frac{\partial w}{\partial z}\psi_i + \frac{\partial w}{\partial z'}\psi_i{}')R\sqrt{1+(R')^2} + Pr'r\psi_i \; dZ \end{array} \right\} = \left\{ \begin{array}{l} 0 \\ 0 \end{array} \right\}. \tag{4.7}$$

The associated algebraic equations (4.7) are solved using a Newton–Raphson procedure.

3.4.2 Results

An initial mass reduction allows a slight bulge under the constant transmural pressure as well as thinning of the wall in the middle of the vessel at $s = 0$. These changes alter stresses from homeostatic values and the lesion starts to enlarge (e.g. see Figure 3.6). Similar to results for saccular aneurysms, a larger value of $\hat{K}_g$ decreases the rate of enlargement of the lesions (Figure 3.7). Here, however, the alignment of new collagen is allowed

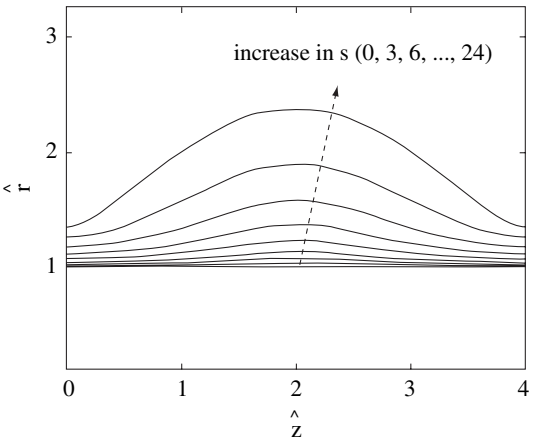

Figure 3.6. Simulation of the enlargement of an axisymmetric fusiform lesion, as a function of nondimensional time $s = t/t_2$, for the case 3 preferred deposition (i.e. preferred direction of new collagen dictated by larger principal stretch) and $\hat{K}_g = 0$.

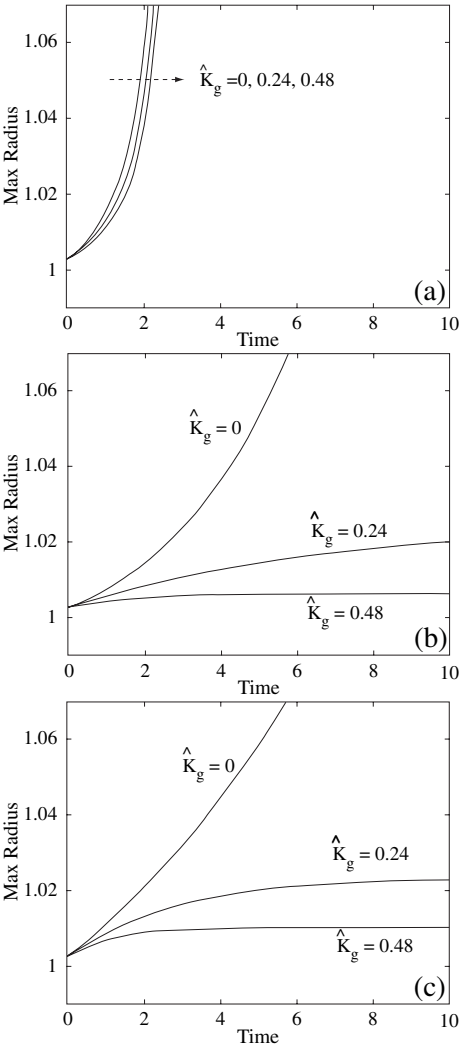

Figure 3.7. Effect of the stress mediation parameter $\hat{K}_g$ on the enlargement of a fusiform lesion due to a 20% initial mass reduction within the central region of the wall and growth and remodeling for different hypotheses on the alignment of newly deposited collagen fibers: (a) case 1; (b) case 2; (c) case 3. Recall that radius and time are nondimensionalized via r/r_h and t/t_2.

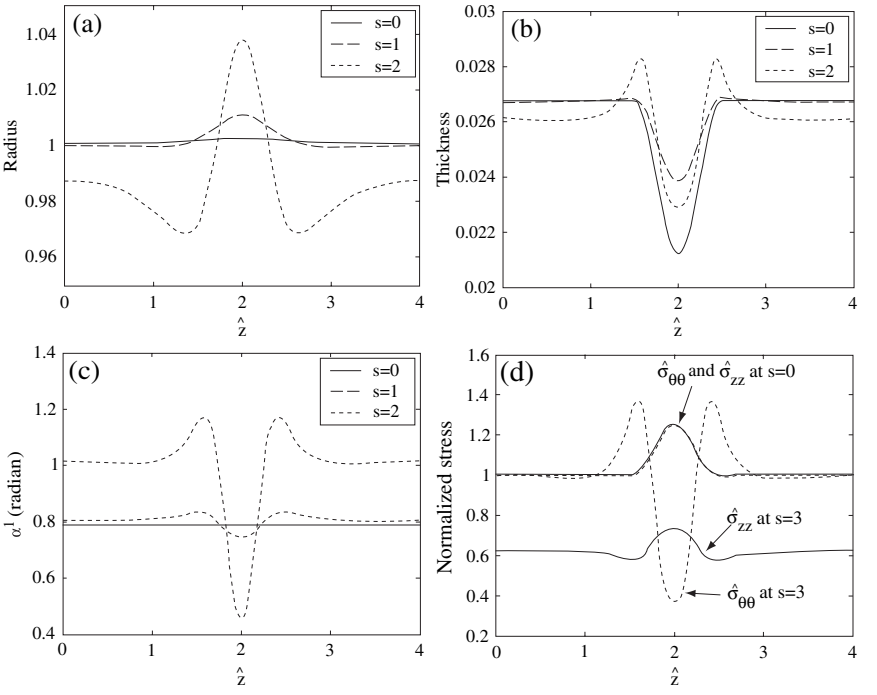

Figure 3.8. Evolution of a fusiform lesion ($\hat{K}_g = 0.48$) with a 20% initial mass reduction within the central region of the wall and case 1 preferred deposition: (a) radius; (b) thickness; (c) fiber orientation of new collagen; (d) principal stresses. The simulation shows that fiber reorientation by case 1 causes an unstable enlargement. Results are similar for $\hat{K}_g = 0$ and 0.24. Recall that radius, thickness, and stress are nondimensionalized via r/r_h, h/r_h, and σ_{ii}/σ_h $(i = \theta, z)$.

to change corresponding to the stress or strain. When the fiber alignment is assumed according to case 2 or 3, the lesion is stable for $\hat{K}_g = 0.24$ and 0.48 but is unstable for $\hat{K}_g = 0$ (e.g. G&R transitions from unstable to stable at $\hat{K}_g \approx 0.06$ for case 3). For case 1, however, the lesion shows unstable growth for $\hat{K}_g = 0$, 0.24, and 0.48. In this case, the angle between the preferred alignment and z-axis, $\alpha^1(s)$ (note that $\alpha^2(s) = -\alpha^1(s)$), decreases because the principal stress σ_{zz} is slightly higher than $\sigma_{\theta\theta}$ at $s = 0$ (see Figures 3.8(c) and 3.8(d)). Further remodeling causes $\alpha^1(s)$ to decrease in the middle but to increase in other regions ($s = 2$ in Figure 3.8c). Because the principal stress σ_{zz} remains higher than $\sigma_{\theta\theta}$, however, the fiber orientation changes further, which makes the enlargement of the lesion unstable even for higher values of $\hat{K}_g$. In contrast, for the case 2 and 3 preferred depositions, the thickness increases in the center and the stresses

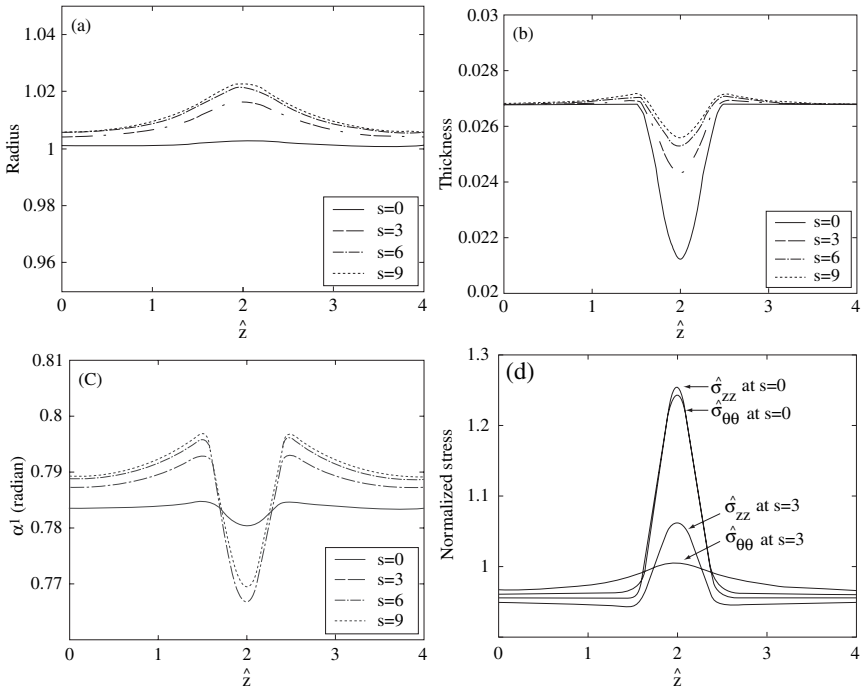

Figure 3.9. Evolution of a fusiform lesion ($\hat{K}_g = 0.24$) with a 20% initial mass reduction and case 3 preferred deposition: (a) radius; (b) thickness; (c) fiber orientation of new collagen; (d) principal stresses. Recall from Figure 3.7 that this is a stable enlargement.

tend to return to the homeostatic value through G&R with $\hat{K}_g = 0.24$ and 0.48 (Figure 3.9). Thus, the postulated alignment of newly deposited collagen fibers had a significant influence on the potential stability of the enlargement.

3.5 Fluid–Solid Interaction

Although conventional analyses of arterial wall mechanics require the deformation to be computed relative to a suitable reference configuration (e.g. a stress-free sector obtained by introducing multiple cuts in an excised segment [HUb,FUa]), the focus of most computational biofluid mechanical analyses is on changes from diastole to systole. Because of the highly nonlinear material behavior of arteries, the deformation from a suitable reference

configuration to an intact diastolic configuration is "large" whereas that from diastolic to systolic is typically "small." Hence, if we know the state of stress in the artery at any configuration between diastole and systole, then the primary need in computational biofluid mechanics is to determine changes in stiffness during the cardiac cycle. We suggest here that the theory of small deformations superimposed on large can be exploited when solving coupled fluid–solid interaction problems during the cardiac cycle. In particular, this approach allows one to include the effects of residual stress, nonlinear material behavior, anisotropy, smooth muscle contractility, and finite deformations of the arterial wall while recovering equations relevant throughout the cardiac cycle that can be solved using methods common to linearized elasticity.

Let the body occupy a configuration $\kappa_{t_o}(\mathcal{B})$ at an intermediate time t_o characterized by a large strain measured from a reference configuration $\kappa_R(\mathcal{B})$. Then, let the position in the intermediate (stressed) configuration be denoted by $\mathbf{x}_o = \chi_{\kappa_R}(\mathbf{X}, t_o)$. Hence, we can consider that a small displacement $\mathbf{u} = \mathbf{u}(\mathbf{x}_o, t)$, superimposed upon the large deformation, yields the "current" position $\mathbf{x}$ at time t, namely

$$\mathbf{x} = \mathbf{x}_o + \mathbf{u}(\mathbf{x}_o, t). \tag{5.1}$$

Deformation gradients associated with mappings from the reference to the intermediate and current configurations are thus given by

$$\mathbf{F}^o = \frac{\partial \chi_{\kappa_R}(\mathbf{X}, t_o)}{\partial \mathbf{X}}, \qquad \mathbf{F} = \frac{\partial \chi_{\kappa_R}(\mathbf{X}, t)}{\partial \mathbf{X}}. \tag{5.2}$$

The deformation gradient representing a mapping from the intermediate configuration to current configurations is similarly,

$$\mathbf{F}^* = \frac{\partial \mathbf{x}}{\partial \mathbf{x}_o} = \mathbf{I} + \mathbf{H}, \qquad \text{where} \quad \mathbf{H} = \frac{\partial \mathbf{u}}{\partial \mathbf{x}_o}. \tag{5.3}$$

The displacement gradient $\mathbf{H}$ can be divided into a symmetric part $\boldsymbol{\epsilon} = \frac{1}{2}(\mathbf{H} + \mathbf{H}^T)$ and a skew-symmetric part $\boldsymbol{\Omega} = \frac{1}{2}(\mathbf{H} - \mathbf{H}^T)$. If $\mathbf{H}$ is small, $\boldsymbol{\epsilon}$ and $\boldsymbol{\Omega}$ are identified as the infinitesimal strain and infinitesimal rotation. Regardless, for the successive motions

$$\mathbf{F} = \mathbf{F}^* \mathbf{F}^o. \tag{5.4}$$

For an isochoric motion, the material is subject to a kinematic constraint: $\det \mathbf{F} = 1$ in general, which reduces to $\mathrm{tr}(\boldsymbol{\epsilon}) = 0$ for an infinitesimal strain. The Cauchy stress $\mathbf{t}$ for an incompressible Green (hyper)elastic material can be written as

$$\mathbf{t} = -p\mathbf{I} + \hat{\mathbf{t}}, \qquad \hat{\mathbf{t}} = \mathbf{F}\hat{\mathbf{S}}\mathbf{F}^T, \qquad \hat{\mathbf{S}} = 2\frac{\partial \hat{W}}{\partial \mathbf{C}}, \tag{5.5}$$

where p is a Lagrange multiplier that enforces the constraint that the motion is isochoric, $\mathbf{C} = \mathbf{F}^T\mathbf{F}$ is the total right Cauchy–Green tensor, and $\hat{\mathbf{t}}$ is the deformation-dependent (or extra) part of the Cauchy stress. For purposes herein, it is convenient to relate $\hat{\mathbf{t}}$ to the extra part of the second Piola–Kirchhoff stress $\hat{\mathbf{S}}$, which in turn is computed directly from a stored energy function $W = \tilde{W}(\mathbf{F})$, or by material frame indifference, $W = \hat{W}(\mathbf{C})$. Now, let the deformation gradient and Cauchy stress of arterial wall in any convenient intermediate configuration during the cardiac cycle be represented by $\mathbf{F}^o$ and $\mathbf{t}^o$ whereas that in any "current" configuration between diastolic and systolic be denoted as $\mathbf{F}$ and $\mathbf{t}$. Using (5.3) and (5.4), (5.5) can be written as

$$\mathbf{t} = -(p^o + p^*)\mathbf{I} + (\mathbf{F}^o + \mathbf{H}\mathbf{F}^o)(\hat{\mathbf{S}}^o + \mathbf{S}^*)(\mathbf{F}^{oT} + \mathbf{F}^{oT}\mathbf{H}^T), \tag{5.6}$$

where

$$\mathbf{S}^* = \frac{\partial \hat{\mathbf{S}}}{\partial \mathbf{C}}\Big|_{\mathbf{C}^o}\mathbf{C}^* \quad \text{with} \quad \mathbf{C}^* = 2\mathbf{F}^{oT}\boldsymbol{\epsilon}\mathbf{F}^o. \tag{5.7}$$

Hence, neglecting higher-order terms in the "small displacement gradient" $\mathbf{H}$, (5.6) can be written in terms of physical components of the tensors as (per the usual summation convention)

$$\begin{aligned} t_{ij} = {} & t^o_{ij} + H_{ik}\hat{t}^o_{kj} + \hat{t}^o_{ik}H_{jk} - p^*\delta_{ij} \\ & + 4F^o_{iA}F^o_{jB}F^o_{kP}F^o_{lQ}\frac{\partial \hat{W}}{\partial C_{AB}\partial C_{PQ}}\bigg|_{\mathbf{C}^o}\epsilon_{kl}. \end{aligned} \tag{5.8}$$

Moreover, recalling that $\mathbf{H} = \boldsymbol{\epsilon} + \boldsymbol{\Omega}$, (5.8) can be written as

$$t_{ij} = t^o_{ij} - p^*\delta_{ij} + \mathcal{C}_{ijkl}\,\epsilon_{kl} + \mathcal{D}_{ijkl}\,\Omega_{kl}, \tag{5.9}$$

where

$$\mathcal{C}_{ijkl} = \delta_{ik}\hat{t}^o_{lj} + \hat{t}^o_{il}\delta_{jk} + 4F^o_{iA}F^o_{jB}F^o_{kP}F^o_{lQ}\frac{\partial \hat{W}}{\partial C_{AB}\partial C_{PQ}}|_{\mathbf{C}^o} \tag{5.10}$$

$$\mathcal{D}_{ijkl} = \delta_{ik}\hat{t}^o_{lj} + \hat{t}^o_{il}\delta_{jk}. \tag{5.11}$$

Because $\epsilon_{ij} = \epsilon_{ji}$ and $\Omega_{ij} = -\Omega_{ji}$ $(i \neq j)$, $\mathcal{C}_{\alpha\beta ij}\epsilon_{ij} + \mathcal{C}_{\alpha\beta ji}\epsilon_{ji} = (\mathcal{C}_{\alpha\beta ij} + \mathcal{C}_{\alpha\beta ji})\epsilon_{ij}$ and similarly $\mathcal{D}_{\alpha\beta ij}\Omega_{ij} + \mathcal{D}_{\alpha\beta ji}\Omega_{ji} = (\mathcal{D}_{\alpha\beta ij} - \mathcal{D}_{\alpha\beta ji})\Omega_{ij}$. Finally, let new quantities $\tilde{\mathcal{C}}_{\alpha\beta ij} = \frac{1}{2}(\mathcal{C}_{\alpha\beta ij} + \mathcal{C}_{\alpha\beta ji})$ and $\tilde{\mathcal{D}}_{\alpha\beta ij} = \mathcal{D}_{\alpha\beta ij} - \mathcal{D}_{\alpha\beta ji}$. Now, we see, from (5.9) and (5.11), that the stress response of a nonlinearly elastic material, from a finitely deformed intermediate configuration such as that at the mean arterial pressure in a large artery, depends strongly on the prestress $\mathbf{t}^o$, initial finite deformation $\mathbf{F}^o$, and possibly small rotations $\boldsymbol{\Omega}$. As an example of the linearization, Figure 3.10 shows the pressure and axial forces for both a nonlinear constitutive relation and its linearized elastic response to the radius changes. The radius changes 3.7% during a cardiac cycle, and the linearized elastic response is close to that determined using the finite nonlinearly elastic response within the cardiac cycle.

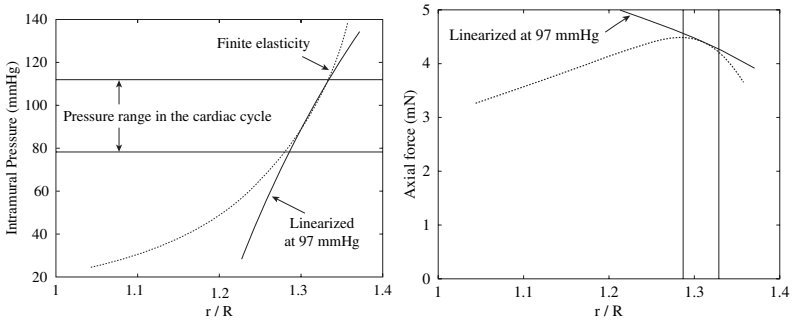

Figure 3.10. Pressure-circumferential stretch (r/R) and axial force-circumferential stretch during inflation at a fixed length. The values are calculated for both the nonlinear and linearized elastic response with respect to the radius changes. The material parameters for the nonlinear response is obtained by a best-fitting to an experimental result of a rabbit basilar artery and the linearized elastic parameters are calculated at 97 mmHg and $\Lambda = 1.3$.

3.6 Discussion

Over the last few decades, many studies have revealed a great deal about the biochemistry related to proteins, DNA, and cell behaviors, and more information is accumulating every day. However, much less is known about how these biochemical and cellular mechanisms result in changes at the organ level. As Hunter and Borg [HUd] emphasized, there is a need to integrate information from proteins to organs, and particularly to develop a framework for computational methods that incorporates biochemical, biophysical, and anatomical information on cells, tissues, and organs. Such frameworks not only integrate information, they also help identify missing data, test hypotheses, and suggest new theoretical and experimental studies. For this purpose, we chose a constrained mixture theory that can model G&R of soft tissue that results from mechanosensitive reactions of cells, including their control of the degradation and deposition of collagen fibers. We specialized the model to a 2-D formulation for the enlargement of intracranial aneurysms with numerical simulations for two idealized geometries: an ellipsoidal shape for saccular aneurysms and a cylindrical shape for fusiform aneurysms. We hypothesized that enlargement results primarily from the coordinated degradation and synthesis of collagen by fibroblasts; moreover, we hypothesized that newly synthesized collagen is incorporated within the wall at a preferred, or homeostatic, deposition stretch. Given these basic

hypotheses, our model predicts that stress-mediated enlargement proceeds via a competition between a local thickening and radial expansion for both saccular and fusiform aneurysms. For a saccular aneurysm, an initially ellipsoidal lesion tends to enlarge toward a spherical shape (Figure 3.4b), which agrees with a statistical study by Parlea et al. [PAa]. For a fusiform aneurysm, we postulated three different hypotheses for the alignment of newly deposited collagen fibers and found that the alignment had a significant influence on the potential stability of the enlargement.

As a first step, it is prudent to use simplified models and idealized geometries to capture salient features of stress-mediated G&R of the aneurysms. In the future, however, we hope to expand the model to incorporate more biochemical, biophysical, and cellular information for G&R of arteries with real anatomical geometries. Also there is no doubt that we have to include fluid–solid interactions for a better understanding. Hence, we suggested that the theory of small on large deformations will be a useful tool for coupled fluid–solid computation within complex geometries.

Acknowledgments This research was supported, in part, by grants HL-64372 and HL-80415 from the NIH.

3.7 References

[CAa] Canham, P.B., Finlay, H.M., Kiernan, J.A., and Ferguson, G.G., Layered structure of saccular aneurysms assessed by collagen birefringence, *Neurol. Res.*, **21** (1999), 618–626.

[CAb] Canham, P.B., Finlay, H.M., and Tong, S.Y., Stereological analysis of the layered collagen of human intracranial aneurysms, *J. Microscopy*, **183** (1996), 170–180.

[DRa] Driessen, N.J.B., Wilson, W., Bouten, C.V.C., and Baaijens, F.P.T., A computational model for collagen fibre remodelling in the arterial wall, *J. Theor. Biol.*, **226** (2004), 53–64.

[FUa] Fung, Y.C., **Biomechanics: Motion, Flow, Stress, and Growth**, Springer-Verlag, New York (1990).

[HOa] Holzapfel, G.A., Gasser, T.G., and Ogden, R.W., A new constitutive framework for arterial wall mechanics and a comparative study of material models, *J. Elasticity*, **61** (2000), 1–48.

[HUa] Humphrey, J.D. and Canham, P.B., Structure, mechanical properties, and mechanics of intracranial saccular aneurysms, *J. Elasticity*, **61** (2000), 49–81.

[HUb] Humphrey, J.D., **Cardiovascular Solid Mechanics: Cells, Tissues, and Organs**, Springer-Verlag, New York (2002).

[HUc] Humphrey, J.D., and Rajagopal, K.R., A constrained mixture model for growth and remodeling of soft tissue, *Math. Models Meth. Appl. Sci.*, **12** (2002), 407–430.

[HUd] Hunter, P.J. and Borg, T.K., Integration from proteins to organs: The Physiome Project, *Nature Rev: Molec. Cell Biol.*, **4** (2003), 237–243.

[KYa] Kyriacou, S.K. and Humphrey, J.D., Influence of size, shape and properties on the mechanics of axisymmetric saccular aneurysms, *J. Biomech.*, **29** (1996), 1015–1022. Erratum, *J. Biomech.*, **30**, 761.

[PAa] Parlea, L., Fahrig, R., Holdsworth, D.W., and Lownie, S.P., An analysis of the geometry of saccular intracranial aneurysms, *Amer. J. Neuroradiol.*, **20** (1999), 1079–1089.

[RAa] Rachev, A., Manoach, E., Berry, J., and Moore, Jr., J.E., A model of stress-induced geometrical remodeling of vessel segments adjacent to stents and artery/graft anastomoses, *J. Theore. Biol.*, **206** (2000), 429–443.

[ROa] Rodriguez, E.K., Hoger, A., and McCulloch, A.D., Stress-dependent finite growth in soft elastic tissues, *J. Biomech.*, **27** (1994), 455–467.

[SAa] Saravanan, U. and Rajagopal, K.R., A comparison of the response of isotropic inhomogeneous elastic cylindrical and spherical shells and their homogenized counterparts, *J. Elasticity*, **71** (2003), 205–233.

[SKa] Skalak, R., Growth as a finite displacement field, in *Proc. IUTAM Symp. on Finite elasticity*, Carlson, D.E. and Shield, R.T., Eds. Martinus Nijhoff (1981).

[TAa] Taber, L.A., A model for aortic growth based on fluid shear stresses and fiber stresses, *ASME J. Biomed. Eng.*, **120** (1998), 348–354.